Journal of Non-Newtonian Fluid Mechanics 166 (2011) 1100–1115

Contents lists available at ScienceDirect

Journal of Non-Newtonian Fluid Mechanics

journal homepage: http://www.elsevier.com/locate/jnnfm

Numerical simulations of mounding and submerging flows of shear-thinning jets impinging in a container ☆

Scott A. Roberts *, Rekha R. Rao

Thermal and Fluid Processes Department, Sandia National Laboratories, Albuquerque, NM 87185, United States

ARTICLE INFO

Article history:
Received 7 October 2010
Received in revised form 23 March 2011
Accepted 13 June 2011
Available online 22 June 2011

Keywords:
CFD
Finite element method
Free surface flow
Jet
Non-Newtonian
Shear-thinning

ABSTRACT

Continuous jets of non-Newtonian fluids impinging on a fluid surface exhibit instabilities from jet buckling and coiling at low Reynolds numbers to delayed die swell, mounding, and air entrainment at higher Reynolds numbers. Filling containers with complex fluids is an important process for many industries, where the need for high throughput requires operating at high Reynolds numbers. In this regime, air entrainment can produce a visually unappealing product, causing a major quality control issue. Just prior to the onset of air entrainment, however, there exists an ideal filling regime which we term "planar filling," as it is characterized by a relatively flat free surface that maintains its shape over time. In this paper, we create a steady-state, 2-D axisymmetric finite element model to study the transition from planar filling to the onset of air entrainment in a container filling process with generalized-Newtonian fluids. We use this model to explore the operating window for Newtonian and shear-thinning (or, more generally, deformation-rate-thinning) fluids, demonstrating that the flow behavior is characterized by a balance between inertial, viscous, and gravitational forces, as characterized by the Reynolds and Froude numbers. A scaling analysis suggests that the relevant parameters for calculating these dimensionless numbers are located where the jet impacts the liquid surface, and simulations show that the transition from planar filling to air entrainment often occurs when $\mathrm{Re} \sim O(10)$. We found that the bottom and side surfaces of the container drastically influence this transition to entrainment, stabilizing the flow.

1. Introduction

A jet of a rheologically complex fluid impinging onto a liquid surface can exhibit a variety of flow regimes, including jet dripping and pinch-off [1–4], hydraulic jumps [5,6], buckling, coiling, and mounding [7–16], and submerging flow and unstable air entrainment [17–21]. This range of behavior has implications in many industrial applications, such as the filling of bottles and containers. Understanding this behavior is especially important in industry, where the fluids filling containers are often highly non-Newtonian, exhibiting some combination of viscoelastic, shear-thinning, and yield-stress properties. Overall product appearance, such as the absence of air bubbles in a transparent product, is highly important.

The production capacity of industrial plants is often limited by the speed at which containers can be filled. Containers often have labels applied before filling, and in some cases containers are already loaded in cardboard boxes, leading to a low tolerance of container over-fill or of product splashing out of the container. Regulations in some regions limit the amount of void space at the tops of container, requiring a precise fill process [22]. Precise filling also allows the use of smaller containers, saving container and transportation costs. Sales of some products also rely on their clarity, and any entrained air bubbles can detract from their appearance. For these and other reasons, it is of great interest to understand the operating conditions that lead to the various flow profiles seen in container filling processes, especially for complex fluids. This understanding will allow an increase in throughput while meeting product quality constraints.

Fig. 1 shows four experimental flow regimes found in container-filling processes. The two regimes of most interest are mounding and air entrainment. While a mounding flow can be seen in Fig. 1b, the air entrainment regime is inherently unsteady and a snapshot is not shown in Fig. 1. At relatively low jet velocities, complex fluids often exhibit mounding behavior, where the jet diameter greatly increases as it nears the liquid pool. These mounds can be stable or unstable, forming ripples, coils, or buckles, all of which may entrain air. These mounds may also grow very tall, reaching the top of the container before the sides completely fill. Taylor [24] discovered this phenomenon in experiments from the late 1960s. Over a decade later, [7,8] performed an extensive experimental investigation into this behavior for Newtonian, viscous jets, finding the jet length-to-diameter ratio, H/D, to be a key physical parameter in determining buckling behavior. Surface tension was found to play a significant

☆ This paper was submitted as part of the special issue of JNNFM from the XVIth International Workshop on Numerical Methods for Non-Newtonian Flows.

* Corresponding author. Tel.: +1 505 844 7957; fax: +1 505 844 4507.
E-mail address: sarober@sandia.gov (S.A. Roberts).

0377-0257/$ - see front matter © 2011 Elsevier B.V. All rights reserved.
doi:10.1016/j.jnnfm.2011.06.006

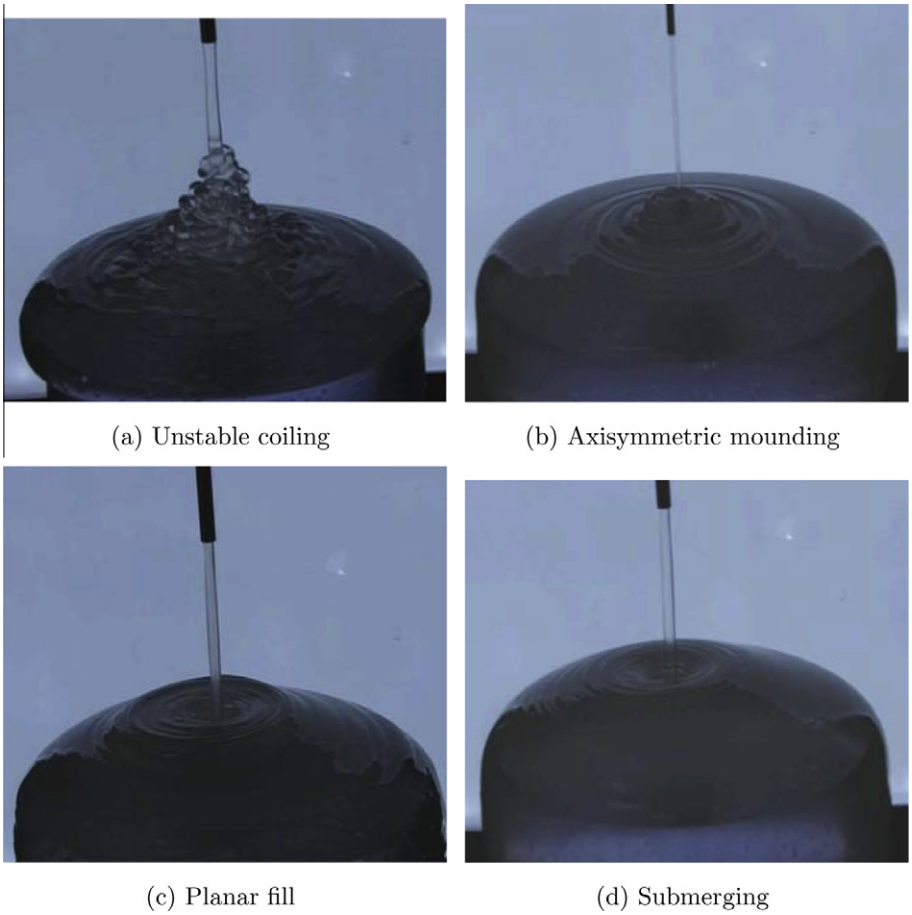

Fig. 1. Experimental images of a sample shear-thinning fluid jet, illustrating the different flow regimes that are often seen in container-filling processes [23]. Nozzle velocity is increasing with each successive image.

role in stabilizing the jet, while the Reynolds number (which is the ratio of inertial to viscous forces) must be low enough ($Re < 1.2$) to ensure that inertia does not overpower the viscous and surface tension stresses, preventing the buckling instabilities. The Reynolds number, along with other relevant dimensionless numbers, are discussed in more detail in Section 3.

Theoretical analysis of unstable mounding flows was first performed by [9], who compared a one-dimensional model for coiling with experimental results [7]. This has been an active area of research since that time, including recent experimental and theoretical efforts [10–16,25], with some studies addressing complex fluids [11]. In particular, [15] used 3-D simulations to model coiling in a container filling process. Container filling in industrial practice, however, normally does not encounter mounding and buckling, due to the high jet velocities, and therefore Reynolds numbers, that are used.

The entrainment of air near the jet impact region occurs at higher Reynolds numbers than mounding behavior and is hence of more practical interest when trying to address container filling throughput. A thorough experimental investigation of air entrainment was first presented by Lin and Donnelly [17,18], who studied the onset of air entrainment for a variety of viscous ($0.9\ \text{cP} < \mu < 400\ \text{cP}$) Newtonian fluids and surfactant mixtures into a large receiving pool. A key finding from this study is a correlation for the minimum air entrainment velocity involving the Weber (which is the ratio of inertial to surface tension forces) and Reynolds numbers, $We = 10Re^{0.74}$. This correlation applies to Newtonian fluids with viscosities in the range of 10–400 cP; in less viscous fluids, such as water, air entrainment only occurs if the jet is perturbed [26]. Over the next few decades, there were a number of experimental studies on air entrainment which are nicely summarized by [19,20]. More recently, experimental work has focused on the rate of air entrainment in laminar and turbulent jets [21,27,28].

Until the late-1990s, there was very little theoretical or computational understanding of submerging jets. Tomé and coworkers [29,30] studied container filling of viscous planar jets with a transient 2-D marker-and-cell numerical method, validated by experiments [30]. While [29] focused on stable filling and buckling, [30] showed two higher velocity regimes, deemed splashing and spluttering. This numerical method was then modified to admit axisymmetric flows [25] and was used to model the filling of cylindrical tubs and containers. Later, this numerical method was again extended to 3-D, allowing the study of arbitrarily shaped jets in addition to planar and axisymmetric ones [10]. The focus of these papers, however, was primarily on the development of the numerical method, rather than on a parametric analysis of the flow regimes. Later, Alexandrou and co-workers used 2-D simulations to observe a wide range of filling regimes for yield-stress materials [31,32]. All of these methods, however, rely on expensive transient simulations, and a quick method of probing a large parameter space would be advantageous.

The previous experiments on high-speed flows [17–21,26–28] were all for Newtonian fluids in very large receiving pools, showing the formation of a cusp-like interface from which air bubbles entrained in the liquid. However, the authors of the current work are interested in understanding the physics behind air entrainment for non-Newtonian fluids filling smaller containers. A common non-Newtonian behavior seen in industrial fluids is shear-thinning,

where the viscosity decreases under applied shear. Those fluids are often modeled with power-law or Carreau models [33]. Shear-thinning models are easily fit to rheological data and have been used extensively to study flows involving free surfaces [1–4,34–40]. These computational studies include film flows [34,35], stability analyses [36,37], coating flows [38–40], and jet pinch-off [1–4], among others. Recent experiments for shear-thinning fluids in a confined geometry shown in Fig. 1, show the full range of filling behaviors, including unstable coiling (Fig. 1a), axisymmetric mounding (Fig. 1b), planar filling (Fig. 1c), and submerging (Fig. 1d) [23].

For the high filling speeds of interest (above the coiling regime), the observed fluid profile is generally axisymmetric, thus a 2-D axisymmetric model can provide insight into these phenomena while reducing computational effort as compared to a 3-D model. While some may refer to this geometry as 3-D axisymmetric [41], we will use the phrase 2-D axisymmetric to make clear that we utilize a 2-D computational mesh to solve this axisymmetric problem. Although the filling of a container is an inherently transient process (the container becomes more full and the fluid interface approaches the top of the container), the experiments shown in Figs. 1b–d are used in industry to investigate flow regimes in container filling processes. The steady-in-time nature of the interface profiles in these images suggest that a steady-state model may be able to capture the correct interfacial profiles with a significant reduction in computational expense over transient simulations.

Therefore, in this paper we present a steady-state, 2-D axisymmetric finite element model (FEM) to study the transition from mounding flow to the onset of air entrainment in confined, container-like geometries. This reduced-order model (as compared to a fully transient 3-D model) will provide practitioners with the ability to perform a computation that runs quickly on an inexpensive workstation and allows exploration of a wide range of operating conditions for a specific process. We use the model to develop operability windows in terms of dimensionless parameters, which can be used for process design.

This paper is organized as follows. In Section 2, we describe the governing equations, geometry, and computational methods used for this study. A scaling analysis is performed in Section 3 to determine the relevant dimensionless parameters. In Section 4, we then proceed with a systematic study of the geometric and rheological parameters, first studying Newtonian fluids, then probing a shear-thinning fluid. Finally, in Section 5, we present our conclusions.

2. Model

In this section, we first present the physical governing equations for Newtonian and shear-thinning fluids (Section 2.1). We then show the container-like geometry (Section 2.2) and boundary conditions for that geometry (Section 2.3). Finally, we show details of the finite element method and solution strategy that is used (Section 2.4).

2.1. Governing equations

Fluid flow is governed by the Cauchy momentum equation and the mass conservation equation for an incompressible liquid,

$$\rho\left(\frac{\partial \mathbf{v}}{\partial t}+\mathbf{v}\cdot\nabla\mathbf{v}\right)=-\nabla p+\nabla\cdot\boldsymbol{\tau}+\rho\mathbf{g}, \tag{1}$$

$$\nabla\cdot\mathbf{v}=0, \tag{2}$$

where the fluid stress tensor is given by $\boldsymbol{\tau}=\left[\mu(\dot\gamma)\left(\nabla\mathbf{v}+(\nabla\mathbf{v})^{\mathrm{T}}\right)\right]$. In these equations $\mathbf{v}$ is the velocity, p the pressure, ρ the density, $\rho\mathbf{g}$ the gravitational force, $\mu(\dot\gamma)$ the apparent viscosity, and t is time. Here we use a generalized-Newtonian viscosity that is a function of the shear rate, $\dot\gamma=\sqrt{\frac{1}{2}\mathrm{trace}(\mathbb{D}\cdot\mathbb{D}^{\mathrm{T}})}$, which is the second invariant of the rate-of-strain tensor, $\mathbb{D}=\nabla\mathbf{v}+(\nabla\mathbf{v})^{\mathrm{T}}$ [33]. The dynamics of the surrounding air phase are neglected, as its viscosity and density are small compared to the fluid.

In this paper, we consider two models for the fluid rheology. The simplest of these is the Newtonian fluid with constant viscosity,

$$\mu(\dot\gamma)=\mu_{\mathrm{newt}}, \tag{3}$$

where μ_{newt} is the Newtonian viscosity. Many fluids with microstructure, such as surfactant solutions and suspensions, exhibit shear-rate dependent behavior. This behavior can be captured by a shear-thinning model, such as the Carreau–Yasuda model [33]. Some publications [1,3,4] use the more general phrases "deformation-rate" and "deformation-rate-thinning" to encompass both the shearing and extensional flows that are observed in our problem. However, we have chosen to use the more conventional phrases "shear-rate" and "shear-rate-thinning" to describe these deformations. The Carreau–Yasuda model is shown in Fig. 2 and defined by

$$\mu(\dot\gamma)=\mu_\infty+(\mu_0-\mu_\infty)\left(1+(\lambda\dot\gamma)^a\right)^{\frac{n-1}{a}}. \tag{4}$$

This model exhibits a zero-shear viscosity plateau at low shear rates, μ_0, an infinite-shear viscosity plateau at high shear rates, μ_∞, and a smoothed power-law behavior in between. Three parameters govern the thinning region; $1/\lambda$ is a characteristic shear rate governing when the transition between μ_0 and the power-law region takes place, n is the shear-thinning parameter or power-law index, which can take values between 1 (Newtonian) and 0 (infinitely thinning) and determines the slope of the power-law region, and a is a parameter governing the smoothness of the transition. In this paper, all fluids are assumed to have a density of $\rho=1$ g/cm^3 and surface tension $\sigma=22$ dyne/cm.

2.2. Geometry

A schematic of the geometry used for this study is shown in Fig. 3. The geometry consists of an overflowing container and a nozzle, and is characterized by a number of parameters, including the total nozzle height, H, nozzle radius, r, container radius, W, and container height, L. The height of the nozzle above the container is $h = H - L$, and the nozzle diameter, $D = 2r$, is often used. Fluid flows out of the nozzle into the container, where it can then overflow the container and run down its sides. This geometry is aligned vertically, such that the nozzle and container axes are aligned with the z coordinate, with gravity aligned in the negative z direction $\mathbf{g}=-g\mathbf{e}_z$. Here, $\mathbf{e}_i$ is the coordinate vector in the i direction.

This geometry was chosen to mimic a filling container, while still allowing a steady-state calculation, due to the fluid

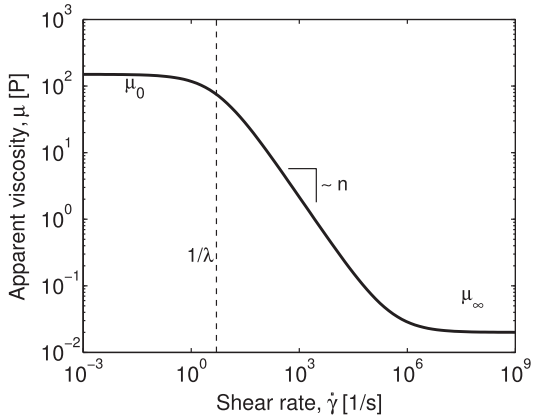

Fig. 2. Plot of the viscosity curve for the Carreau–Yasuda model used in this study. Base case parameters (also found in Table 1) are $\mu_0 = 150$ P, $\mu_\infty = 0.02$ P, $n = 0.2$, $\lambda = 0.2$ s, and $a = 0.8$.

overflowing the cup. This geometry is consistent with the experimental geometry used in industry for similar studies (Fig. 1). In Section 4, we show that this geometry can reasonably be used to study transient container-filling processes.

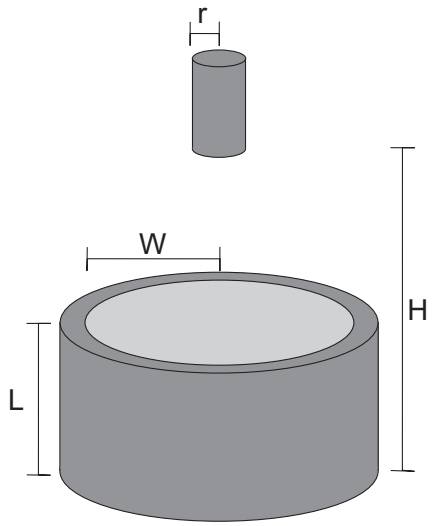

Fig. 3. Schematic of the nozzle/container geometry. Key physical parameters are labeled. In the base case (found in Table 1), $L = 3$ cm, $H = 9$ cm, $W = 6$ cm, $r = 0.3$ cm.

2.3. Boundary conditions

A number of boundary conditions are specified for the solution of this problem. At all fluid-solid boundaries, such as the container sides and bottom and the nozzle walls, no-slip and no-penetration conditions are appropriate, $\mathbf{v} = \mathbf{0}$. The velocity at the nozzle inlet (top) is specified to be a uniform velocity field $\mathbf{v} = -V\mathbf{e}_z$ with V as the mean nozzle velocity. We have ensured that the nozzle is long enough to obtain a fully-developed Poiseuille flow field upon exiting the nozzle.

Free fluid-air interfaces are governed by a balance of normal stresses across the interface, $\mathbf{n} \cdot \boldsymbol{\tau} = 2\kappa\sigma\mathbf{n}$, which introduces capillary effects into the problem. In this equation, $\mathbf{n}$ is the outward pointing normal vector to the interface, κ is the interfacial curvature, $\kappa = \nabla_s \cdot \mathbf{n}/2$, and σ is the interfacial tension. The operator ∇_s is the surface gradient operator, defined as $\nabla_s f = (\mathbb{I} - \mathbf{nn}) \cdot \nabla f$. The location of the free interface is evolved with a kinematic boundary condition, $\mathbf{n} \cdot (\mathbf{v} - \mathbf{v}_s) = 0$, while conditions of axisymmetry are applied at the internal symmetry boundaries. Here, $\mathbf{v}_s$ is the velocity of the interface. At steady-state, $\mathbf{v}_s = 0$, leading to the simplified kinematic condition $\mathbf{n} \cdot \mathbf{v} = 0$.

2.4. Computational method

This model consists of a 2-D axisymmetric mesh, shown in Fig. 4. The mesh is comprised of unstructured quadrilateral elements created using a combination of domain mapping and paving

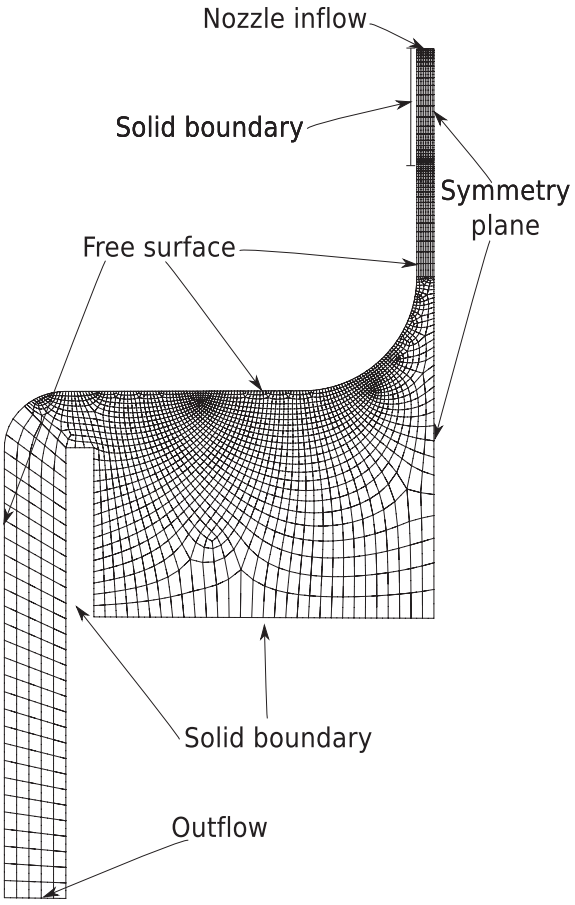

(a) Undeformed initial guess, with labeled boundary conditions

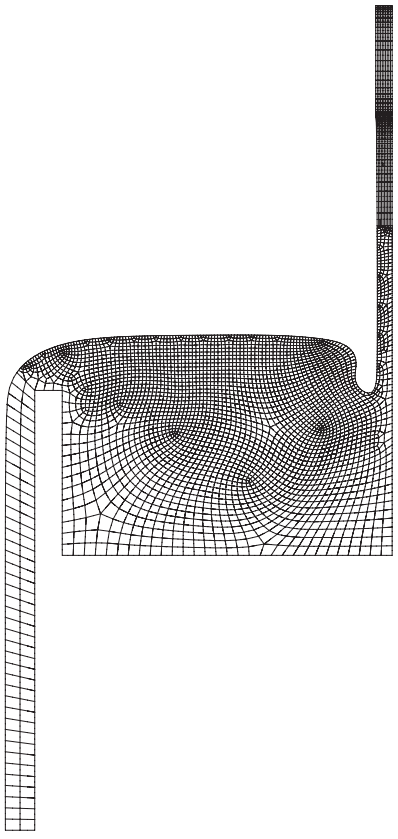

(b) Deformed mesh for a typical submerged jet

Fig. 4. Sample 2-D axisymmetric mesh for the geometry described in Fig. 3.

methods and generated by Cubit [42]. The equations are discretized with the Galerkin finite element method (FEM) using an arbitrary Lagrangian-Eulerian (ALE) scheme [43,44] to accommodate movement of the mesh. This method was pioneered by Scriven and coworkers for coating-related problems [45–47], and has since been used to solve a number of free surface flows, including drop dynamics [48–51] and liquid bridges [52,53]. The mesh is modeled as a computational Lagrangian solid, following the momentum balance for a quasi-static elastic solid,

$$\mathbf{V}\cdot\mathbb{T}=0, \tag{5}$$

where $\mathbb{T}$ is the total pseudo-solid stress, given by the neo-Hookean constitutive equation [43]. The mesh boundaries of free fluid-air interfaces are located with the kinematic boundary condition, $\mathbf{n}\cdot(\mathbf{v}-\mathbf{v}_s)=0$, while conditions of axisymmetry are applied at the internal symmetry boundaries. Here, $\mathbf{v}_s$ is the velocity of the interface and $\boldsymbol{n}$ is its outward pointing normal vector.

All of these computations are performed in Goma, a full-Newton FEM code developed by Sandia National Laboratories [54]. Goma has been used to solve a wide variety of free-interface problems, including those with shear-thinning rheology [55,56]. Solution of the resulting linear matrix system is performed in Trilinos [57] using the SuperLU_DIST parallel direct solver [58]. Simulations were performed in parallel on a modern quad-core processor. Performance of this method is briefly discussed in A.3.

As the desire is to calculate a steady-state solution for the interfacial and velocity profiles, an initial guess is required for the interfacial profile, velocities, and pressure. The initial guess for the interfacial profile is a simplified jet generated in Cubit [42] using simple geometric components. Shown in Fig. 4a, this profile has the jet smoothly flowing into the pool and overflowing the container. The initial guess for the velocities and pressure is zero. Further details on the convergence and refinement of the mesh are included in A.1.

Throughout this paper, results are presented in terms of the minimum nozzle velocity required to obtain a given flow profile or transition. This nozzle velocity will be characterized by a "critical velocity" or "critical Reynolds number." To determine this velocity, a first-order continuation method is used. The solution is first converged at a relatively low velocity. Then, a series of steady-state solutions are obtained by incrementing the velocity using first-order continuation [59],

$$\mathbf{x}^{\text{guess}}(V^{\text{new}})=\mathbf{x}^{\text{old}}(V^{\text{old}})+\Delta V\frac{\partial\mathbf{x}}{\partial V}, \tag{6}$$

where $\boldsymbol{x}$ is the solution vector and V is the nozzle velocity. $\mathbf{x}^{\text{guess}}$ is used as the initial guess for each subsequent solution. This procedure is continued until the desired interface profile is achieved. The full details of the continuation algorithm, including convergence of the initial profile, are included in A.2.

3. Scaling analysis

While the numerical computations described in Section 2 are conducted using the full dimensional form of the governing equations, additional physical insight may be gained by defining a consistent set of characteristic dimensional parameters to use in analyzing the computational data. A naïve approach to this may be to use the most obvious scales, the mean nozzle velocity V and nozzle diameter D for velocity and length scales and the Newtonian viscosity for viscous scalings. For a shear-thinning fluid, the choice of a viscous scaling becomes more difficult, as there are many options (zero-shear viscosity, infinite-shear viscosity, or something in between). A non-dimensionalization based on these parameters and a pressure scaled with an inertial scaling (ρV^2) yields a dimensionless form of the momentum equation,

$$\frac{D\mathbf{v}}{Dt}=\frac{1}{\overline{\text{Re}}}\nabla\cdot\left[\beta(\nabla\mathbf{v}+(\nabla\mathbf{v})^{\text{T}})\right]-\nabla p+\frac{1}{\overline{\text{Fr}}}\mathbf{g}, \tag{7}$$

where $D\mathbf{v}/Dt=\partial\mathbf{v}/\partial t+\mathbf{v}\cdot\nabla\mathbf{v}$ is the total derivative. Here, β represents the dimensionless Carreau–Yasuda viscosity,

$$\beta=\frac{\mu(\dot\gamma)}{\mu_\infty}=1+(\bar\beta-1)\left[1+(\overline{\text{Wi}}\dot\gamma)^a\right]^{\frac{n-1}{a}} \tag{8}$$

with the viscous term scaled by μ_∞. The normal stress balance also yields a dimensionless form,

$$\mathbf{n}\cdot\tau=2\kappa\mathbf{n}/\text{We}. \tag{9}$$

In (7–9), all variables (such as $\boldsymbol{v}$, p, $\dot\gamma$, and $\boldsymbol{\tau}$) are dimensionless. This scaling yields a number of dimensionless parameters, including the Reynolds number $\overline{\text{Re}}=\rho VD/\mu_\infty$, Froude number $\overline{\text{Fr}}=V^2/gD$, Weber number $\overline{\text{We}}=\rho V^2D/\sigma$, viscosity ratio $\bar\beta=\mu_0/\mu_\infty$, and dimensionless characteristic inverse shear rate for shear-thinning, similar to a Weissenberg number $\overline{\text{Wi}}=\lambda V/D$.

We can imagine that the various length scales present in the problem could be important to stability transitions. This scaling introduces three dimensionless length scales, one of which, h/D, has been shown to be a critical parameter in some regimes [19,20]. Since we have a finite pool depth, where the bottom of the pool will affect the flow, L/D may also be important. Walls introduce another scaling, W/D. Thus, the critical Reynolds number may be function of all of these dimensionless parameters,

$$\text{Re}_{\text{crit}}=f\left(\overline{\text{Fr}},\overline{\text{We}},\overline{\text{Wi}},\frac{h}{D},\frac{L}{D},\frac{W}{D},\bar\beta\right). \tag{10}$$

However, we propose that the important physics in this problem occur where the jet impacts the fluid pool, not in the nozzle. Therefore, it is useful to approximate the relevant values there, rather than those associated with flow in the nozzle. Gravity acts to accelerate, and therefore thin, the jet at it flows towards the bath. This change in velocity can be calculated using Bernoulli's equation[60],

$$\frac{p}{\rho}+gh+\frac{1}{2}V^2=\text{constant}, \tag{11}$$

assuming any changes in pressure are from gravity and the viscous effects are negligible. This yields a jet velocity $V_{\text{jet}}=\sqrt{V^2+2gh}$, where the jet has been accelerated by gravity over the distance of the nozzle height, h. Conservation of mass leads to a jet diameter, $D_{\text{jet}}=D\sqrt{V/V_{\text{jet}}}$. The physical location of these velocity and length scales is shown in Fig. 5. To incorporate shear-thinning effects into the viscosity scale, we must have a characteristic shear rate to use in the Carreau–Yasuda model. The jet velocity and diameter can be used to estimate this characteristic shear rate at impact, $\dot\gamma_{\text{jet}}=V_{\text{jet}}/D_{\text{jet}}$, which can then be used to calculate a characteristic viscosity (for shear-thinning fluids) from (4),

$$\mu_{\text{jet}}=\mu(\dot\gamma_{\text{jet}})=\mu_\infty+(\mu_0-\mu_\infty)\left(1+\left[\lambda\left(\frac{V_{\text{jet}}}{D_{\text{jet}}}\right)\right]^a\right)^{\frac{n-1}{a}}, \tag{12}$$

which captures the localized physics of the jet impact region. This analysis is similar to that presented by [26] for Newtonian fluids.

Using these jet-impact based scales, a new Reynolds number can be defined that more accurately represents the relevant balance for forces at jet impact, $\text{Re}=\rho V_{\text{jet}}D_{\text{jet}}/\mu_{\text{jet}}$. This Reynolds number can then be related back to the naïve parameters defined using geometric and inflow parameters

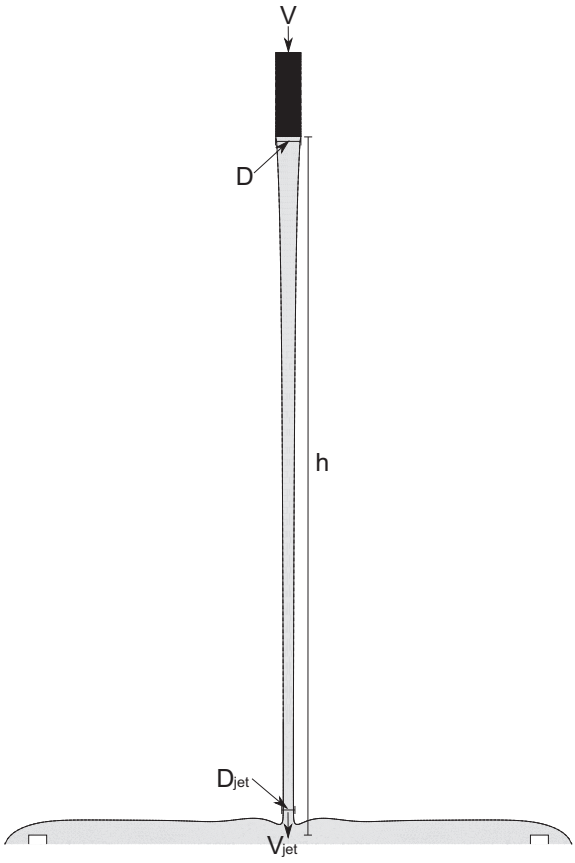

Fig. 5. Schematic of a thinning jet for a large nozzle height. Nozzle inlet scalings, V and D, used to calculate the naïve Reynolds number $\overline{\mathrm{Re}}$ are shown, along with the Bernoulli-based jet scalings, V_{jet} and D_{jet}, used for the impact Reynolds number Re.

$$\mathrm{Re} = \overline{\mathrm{Re}}\left(1 + \frac{2}{\overline{\mathrm{Fr}}}\frac{h}{D}\right)^{1/4}\frac{1}{\hat{\beta}} \tag{13}$$

with a new dimensionless viscosity

$$\hat{\beta} = \frac{\mu_{\mathrm{jet}}}{\mu_\infty} = 1 + (\bar{\beta} - 1)\left(1 + \left[\overline{\mathrm{Wi}}\left(1 + \frac{2}{\overline{\mathrm{Fr}}}\frac{h}{D}\right)^{3/4}\right]^a\right)^{\frac{n-1}{a}}. \tag{14}$$

From (13), two different regimes of Froude number dependence are observed. For large Froude numbers, we will see a dependence only on the inflow Reynolds number, $\overline{\mathrm{Re}}$, and the dimensionless characteristic shear rate, $\overline{\mathrm{Wi}}$. In this limit, $\mathrm{Re} = \overline{\mathrm{Re}}/\hat{\beta}$. At small Froude numbers, the dimensionless length-scale, h/D, becomes more important. As is shown in Section 4, Froude numbers in this study range from 10^{-2} to 10^2, so a combination of these limiting behaviors will be observed.

Eq. 13 also suggests alternative scalings for the other dimensionless parameters in (10). The Froude number is first redefined to be based on the nozzle height rather than the diameter, $\mathrm{Fr} = \overline{\mathrm{Fr}}(h/D) = V^2/gh$. The dimensionless characteristic inverse shear rate can also be redefined using the alternative scaling as $\mathrm{Wi} = \overline{\mathrm{Wi}}(V_{\mathrm{jet}}/V)(D/D_{\mathrm{jet}}) = \lambda V_{\mathrm{jet}}/D_{\mathrm{jet}}$. The remaining length scales can also be made dimensionless by the jet-based diameter, such as L/D_{jet}. We use these definitions of the dimensionless parameters in the remainder of our analysis.

Due to the presence of a free surface in this problem, one may be interested in the importance of capillary forces in this analysis. A calculation of the Weber number yields the relative importance of inertial forces to surface tension forces. Calculation of the Weber number for the data presented in Section 4 yields a range of $15 < \mathrm{We} < 430$, all of which suggest that inertial forces should dominate over surface tension forces. Indeed, upon examining the data using the Weber (or Capillary) number, no correlation was found. Therefore, we do not further explore surface tension effects here.

4. Results and discussion

As the purpose of this study is the identification of an ideal operating regime for container filling processes that is free of air entrainment, we must first identify the flow regimes which will be used to characterize these flows. Fig. 6 illustrates four distinct regimes, all of which were calculated using the base state rheology and geometry, which is set forth in Table 1. The lowest velocity regime, shown in Fig. 6a, is characterized by a widening of the jet diameter prior to joining the liquid pool and is known as "mounding." In this regime, which is at higher velocities than coiling flows occur [7,8], the flow is stable and does not entrain air, although the velocity is slower than desired for most filling processes. This regime can lead to container under-filling or overflowing of the container, if the mound reaches the top of the container before the sides have filled. The second regime (Fig. 6b) is a transitional flow deemed the "planar flow." As it is fast enough to be of practical interest, yet still slow enough to not threaten air entrainment, it is an ideal operating condition. This flow is signaled by a sharp transition from a jet of nearly constant diameter to a relatively flat pool, with no mounding or submerging observed. As the velocity continues to increase, the jet begins to submerge into the fluid pool, as illustrated in Fig. 6c. While this "submerging" regime does show that the jet does reach lower than the top of the pool and air is present below the liquid interface, full 3-D transient simulations (discussed later) suggest that this flow is stable and the air layer surrounding the jet does not entrain air bubbles into the pool. Finally, a critical flow profile, deemed "entrainment," is reached where the air layer becomes unstable and the edge of the fluid pool curls over towards the jet at the point of entry (Fig. 6d). At this point, the submerged interface of the fluid pool is parallel to the jet. While [21] show stable flow profiles that are clearly past this regime, the thin air layers shown would be extremely sensitive to small perturbations and are therefore not suitable for high-speed, vibration-prone filling operations. Therefore, this curl-over regime will be used to signal the beginning of air entrainment.

While these guidelines for determining flow regimes are reliable, each flow profile looks slightly different and identification of the regimes can be subjective. In particular, differences in the details of the surface profile can lead to some uncertainty in determining the planar-flow transition. These uncertainties may lead to some of the data scatter seen in the results presented in this section.

The flow profiles generated from our model can be easily visualized; Fig. 7a shows velocity streamlines for a sample submerging flow. The streamlines show that the jet is moving at a very high speed, and that the velocity decreases sharply as soon as the jet impacts the pool. The viscous forces then dissipate the momentum from the liquid jet both radially and axially. Fluid leaving the container speeds up slightly, then develops a laminar film-flow profile down the outside of the container. The corresponding pressure field is shown in Fig. 7b, where the pressure is lowest where the jet leaves the nozzle, as it is in extension, and rises throughout the falling jet, reaching a local maximum at impact.

While an extensive verification and validation study of our model was not performed, the model does qualitatively agree with interface profiles of similar geometries generated computationally, as summarized in Fig. 8. Transient 3-D simulations were performed using two methods. First, FLOW-3D [61] was used to model the current "overflowing cup" geometry in a transient 3-D simulation.

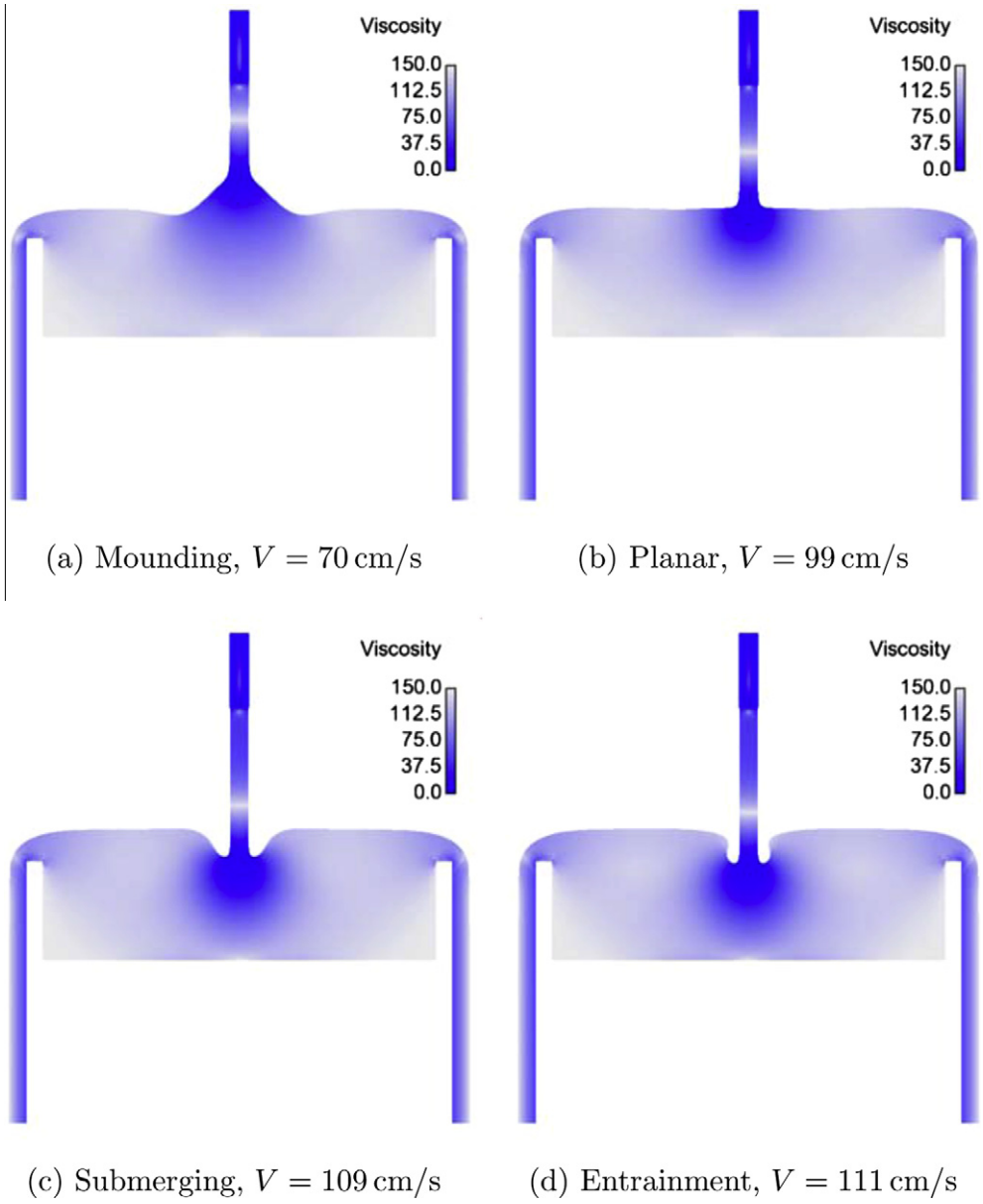

Fig. 6. Illustration showing the various flow regimes for the model shear-thinning fluid of Fig. 2. The nozzle velocity is increasing in successive images, other parameters having the base case values, given in Table 1. The color function is the apparent viscosity, $\mu(\dot{\gamma})$ (in units of Poise).

Table 1
Base case values for rheological and geometric parameters. The parameter values are used for all simulation results, unless otherwise specified.

Parameter name	Symbol	Value
Density	ρ	1 g/cm^3
Surface tension	σ	22 dyne/cm
Zero-shear viscosity	μ_0	150 P
Infinite-shear viscosity	μ_∞	0.02 P
Power-law index	n	0.2
Inverse characteristic shear-rate	λ	0.2 s
Transition parameter	a	0.8
Container height	L	3 cm
Nozzle height, total	H	9 cm
Container radius	W	6 cm
Nozzle radius	r	0.3 cm

This simulation was allowed to run until it reached a steady-state profile, and the results for two nozzle velocities are shown in Figs. 8b and e. Second, OpenFOAM [62] was used to run a simulation in a tall cylindrical container. As this simulation will never reach a steady state (as the liquid meniscus continues to rise higher in the container with time), a snapshot of the interface profile was taken when the height of the fluid interface was 3 cm, which is the height of the cup in the previous simulations. These profiles are shown in Figs. 8c and f. Comparisons can be made between these transient simulations and the results of our model, for which a 3-D visualization is shown in Figs. 8a and d.

Our simplified model shows an excellent comparison to these transient 3-D simulations in the jet impact region. While the calculations for our model and the FLOW-3D model were performed at identical nozzle velocities, the nozzle velocities required to obtain a similar interface profile were slightly lower in the OpenFOAM simulations. This discrepancy suggests that our model may slightly over-predict the critical nozzle velocities that would occur in a true container. However, results from these and other simulations suggest that the trends that we report in this section are qualitatively correct, even if they are not in exact quantitative agreement.

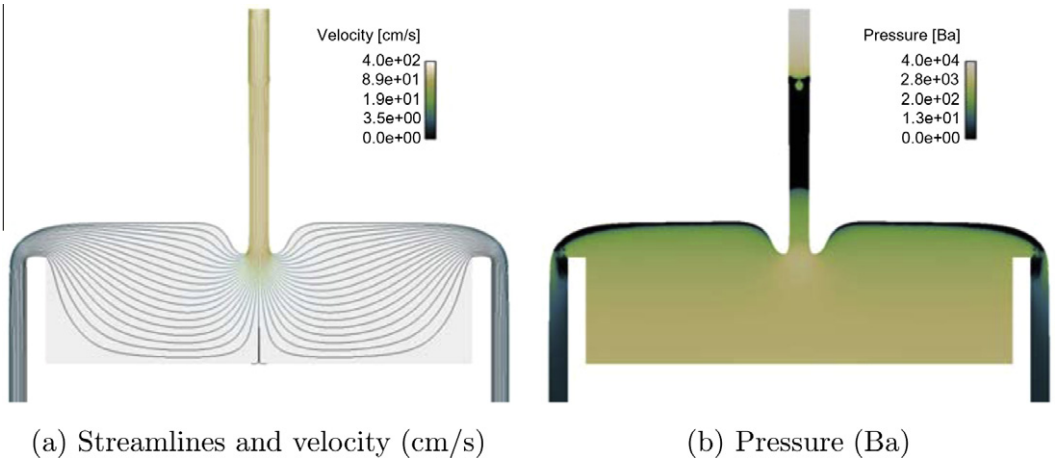

Fig. 7. Typical flow profile for a submerged shear-thinning fluid at the base state parameters in Table 1. In (a), streamlines (colored by the magnitude of the velocity using a logarithmic color scale) show that the flow is quite simple and does not have any recirculation regions. The gray background denotes the interior of the container, where fluid is present. The pressure field is shown using a logarithmic color scale in (b).

Similar interfacial profiles are also observed in experiments with a shear-thinning fluid impinging on a shallow pool, shown in Figs. 1b and d. While the rheology and operating parameters are not identical between the computations shown in Fig. 8 and these experiments, the general trends observed hold. All four regimes have been similarly observed experimentally, and the interface profiles are consistent with those shown by Tomé and coworkers [10,29,30].

In the following presentation of our analysis, we discuss the results in terms of the four flow regimes previously identified (mounding, planar, submerging, and entraining). We will primarily focus on the two transition regimes, planar flow and entrainment. One exception to this is Newtonian fluids, which do not readily show mounding behavior. Instead, the impact region of Newtonian jets are always slightly submerged, with no clear transition from a mounding to a submerging profile. Therefore, in our Newtonian analysis, we only discuss the onset of air entrainment.

In the following subsections, we first explore the effect of the container geometry on the flow regimes for Newtonian fluids, also analyzing the effect of the Newtonian viscosity on entrainment behavior. We then proceed to shear-thinning fluids, where a thorough investigation of the Carreau model parameters is presented.

4.1. Geometry effects on Newtonian fluids

A key difference between container filling and the experiments of [18] is the geometry; containers present a confined geometry, where the fluid dynamics near the jet impact are strongly influenced by the presence of the bottom and sides of the container. This influence is clearly demonstrated in Fig. 9, where the critical air entrainment velocity is shown for three container radii. In these results, the critical Reynolds numbers are $\mathrm{Re} \sim \mathrm{O}(1)$, while the correlation of [18] predicts $\mathrm{Re} \approx 0.0098$ for the same fluid and nozzle diameter, a difference of two orders of magnitude. We also note that [18] use much less viscous fluids ($0.009\ \mathrm{P} < \mu < 4\ \mathrm{P}$) than are of interest here ($\mu \sim 100$ P), and that the Reynolds number predicted for our fluid is far outside the range of their correlation's data (the lowest Reynolds number in [18] is $\mathrm{Re} \approx 8$).

Not only does the presence of container walls have a significant impact on the critical entrainment Reynolds number, but the distance of the walls from the jet impact also strongly affects this behavior. A clear downward trend in the critical Reynolds number with increasing container radius is shown in Fig. 9. This behavior not only confirms our deviation from the results of [18], but also shows that slight deviations to the radius of the container (think undulations in the contour of the container as it fills) could make a significant difference in the flow regime throughout a filling process.

Besides simple changes to the critical Reynolds number, widening the container beyond $W \approx 6.5$ cm can lead to a drastic change in the flow profile, as shown in Fig. 10. This unconverged simulation for a wide container ($W = 14$ cm) shows the development of a flow recirculation region near the jet impact. This recirculation leads to a drastic change in the interface shape, from the smooth "U"-shaped profile shown in Fig. 7 to the trumpet-shaped profile seen in many previous studies [18,20,21]. All of these previous studies have had very large liquid pools, and the "U"-shaped profile is consistent with previous simulations with confined geometries [30, figure 15]. This recirculation allows the momentum dissipation to take place over a larger area and for the velocity to remain high near the impact region, with fluid particles in the jet plunging deep into the pool before slowing down. This transition in flow profiles from narrow to wide baths illustrates that there is a significant difference between jets impinging in container-like geometry and in an unconfined pool. The substantial modification of the flow profile due to the presence of side walls greatly stabilizes these flows, forcing the onset of air entrainment to higher Reynolds numbers.

Other geometric parameters, such as the bath depth L and nozzle height h, play a role in determining the entrainment velocity. Fig. 11 shows two regimes of behavior for the bath depth. At deeper bath depths ($L/D_{jet} \gtrsim 10$), there is little variation in the critical entrainment Reynolds number, while in shallower pools ($L/D_{jet} \lesssim 10$), there is a sharp increase in the critical entrainment Reynolds number. When the bath is very shallow ($L/D_{jet} \lesssim 10$), the flow in the impact region feels the effect of the container bottom, causing the fluid to spread horizontally, rather than plunging deeper. This spreading motion inhibits the submerging motion, requiring a higher velocity to entrain air. This effect is similar to what was seen with the container radius, shown in Fig. 9. As the bath becomes deeper, the impact region interacts less with the bottom, allowing air entrainment to occur at lower velocities. In industrial container filling operations, this means that when a container is being filled from a nozzle with a constant inlet velocity, air entrainment is more likely to happen late in the filling process, when the bath is deeper, rather than earlier. A possible method of reducing the risk of air entrainment is decreasing the nozzle velocity (and therefore the Reynolds number) throughout the

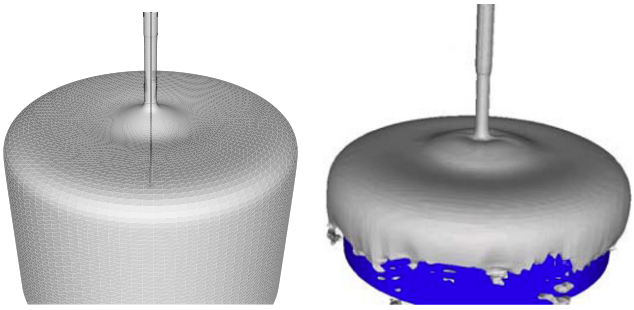

(a) Mounding - model, $V = 140\,\mathrm{cm/s}$

(b) Mounding - FLOW-3D, $V = 140\,\mathrm{cm/s}$

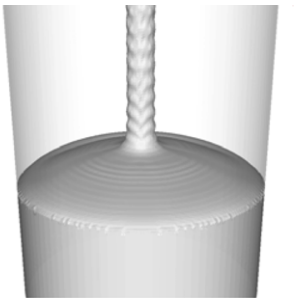

(c) Mounding - OpenFOAM, $V = 130\,\mathrm{cm/s}$

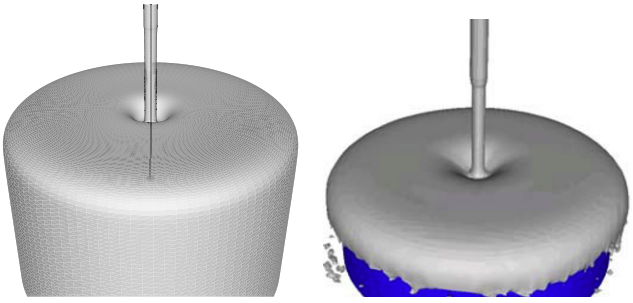

(d) Submerging - model, $V = 150\,\mathrm{cm/s}$

(e) Submerging - FLOW-3D, $V = 150\,\mathrm{cm/s}$

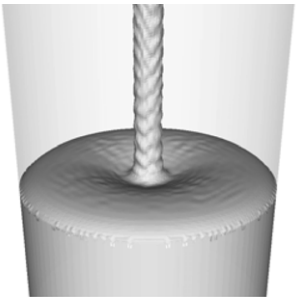

(f) Submerging - OpenFOAM, $V = 140\,\mathrm{cm/s}$

Fig. 8. Comparison of the present model with 3-D transient calculations using FLOW-3D [61] (b, e) and OpenFOAM [62] (c, f). The rheology is described by the Carreau–Yasuda model with $\mu_0 = 214$ P, $\mu_\infty = 0.122$ P, $\lambda = 0.22$ s, $n = 0.2$, and $a = 0.82$ and geometric parameters from Table 1. FLOW-3D calculations are using an overflow geometry identical to the one used in our model, while the OpenFOAM calculations were performed in a cylindrical bottle geometry, and the snapshots are taken when the fluid height is similar to the height in the overflow geometry.

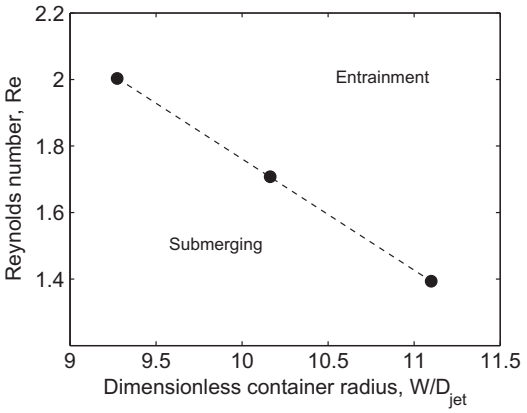

Fig. 9. Effect of container radius (W), made dimensionless by the jet diameter D_{jet}, on critical entrainment Reynolds number, with a linear fit to the data. Simulations are for a Newtonian fluid with $\mu_{newt} = 150$ P. Geometric parameters are $r = 0.3$ cm, $L = 10$ cm, and $h = 10$ cm.

filling process. This would allow a higher velocity early in the filling process and an overall faster container fill than if the nozzle velocity was held constant (at a lower value) throughout the fill.

The nozzle height (h) and diameter (D), along with the fluid viscosity, also play a role in determining the container-filling behavior, as illustrated in Fig. 12. In order to compare the naïve calculation of the nozzle-based dimensionless numbers with our jet-based scalings (calculated in Section 3 from Bernoulli's equation), we show both sets of data in Fig. 12. The nozzle-based parameters, shown in Fig. 12a, show a significant spread to the data, with many values of the Reynolds number appearing for a single Froude number. These data also show a strong trend of higher critical entrainment Reynolds numbers as the Froude number increases. The Bernoulli-based scalings, shown in Fig. 12b, however, are much less dependent on the Froude number. These simulations are for Newtonian fluids with a large range of viscosities ($60\ \mathrm{P} < \mu_{newt} < 160\ \mathrm{P}$) and nozzle velocities ($200\ \mathrm{cm/s} < V < 600\ \mathrm{cm/s}$); however it is important to note that the critical entrainment Reynolds number (jet-based) is relatively constant over this entire range. This behavior is consistent with the scaling analysis of (13), as when $\mathrm{Fr} \gg 1$ we do not expect the Reynolds number to have a Froude number dependence. There is only a slight dependence on the Froude number with this data ($\mathrm{Re} \sim \mathrm{Fr}^{-0.05}$). This relatively constant scaling allows us to conclude that the onset of air entrainment is governed by a balance between the inertial forces of the jet and the momentum dissipation in the liquid pool. It also reinforces our assertion that the correct scaling for our equations are indeed based on the jet properties near the impact region, as estimated using the Bernoulli scalings introduced in Section 3. One caveat to this behavior is for $h = 3$ cm, shown with the open symbols in Fig. 12b. At this height, the nozzle is so close to the bath impact region that the presence of the nozzle itself interferes with the jet behavior. The jet immediately slows and expands as soon as it leaves the nozzle, and does not develop the thinning jet profile used in the development of (13). If these outlying points are ignored, the scatter of these data is significantly less than in the nozzle-based scalings.

4.2. Shear-thinning fluids

A key motivation of this work is understanding the flow regimes for shear-thinning fluids and how the Carreau model parameters affect the flow. In Section 4.1, we showed that the Reynolds number is a good metric for understanding and predicting the onset of air entrainment in Newtonian fluids. In this section, we use the Carreau–Yasuda model (4) to study the transitions from planar

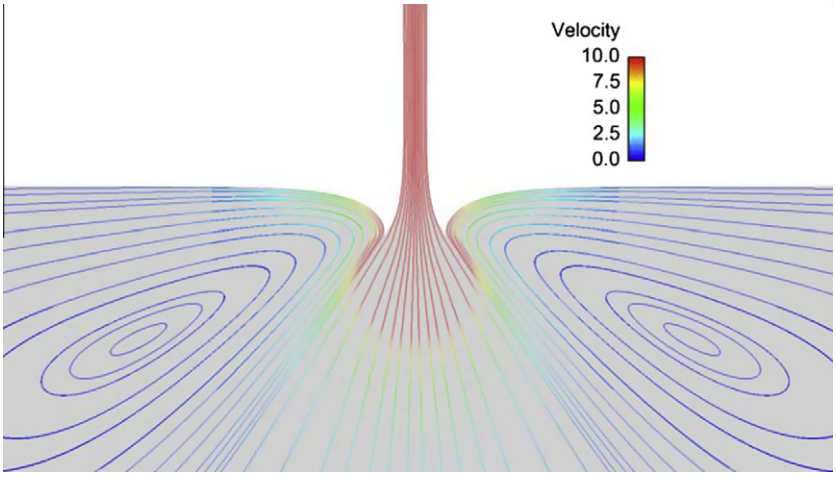

Fig. 10. Unconverged simulation of the jet impact region for a Newtonian simulation with a wide container, $W = 14$ cm. Interface profile shows the emergence of the trumpet-like profile seen in previous studies [18,20,21]. Streamlines are shown colored by the magnitude of the velocity (in units of cm/s), illustrating that this trumpet-like profile is due to the recirculation zones present, in contrast with the steady flow of confined geometries shown in Fig. 7. Rheological parameters are the same as in Fig. 9.

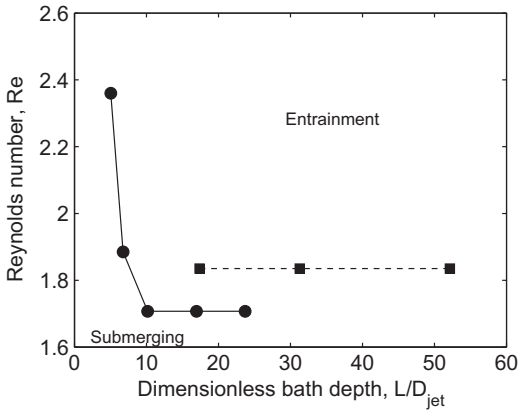

Fig. 11. Effect of bath depth (L), made dimensionless by the jet diameter D_{jet}, and nozzle height (h) on critical entrainment Reynolds number. Circles are at $h = 6$ cm and squares are at $h = 18$ cm. Both sets are for Newtonian fluids with $\mu_{newt} = 150$ P and geometric parameters from the base case in Table 1.

flow to air entrainment of shear-thinning fluids. We use the Reynolds number to characterize the ideal operating window for these fluids. Such a model is appropriate for many micellar solutions.

Before addressing the characteristic parameters of shear-thinning fluids, we must first understand any qualitative differences between Newtonian and shear-thinning fluids and determine what role the nozzle geometry plays. This issue of nozzle height and diameter is addressed in Fig. 13, where we use the Reynolds number to parametrize the transition regimes (planar-flow and air entrainment) for the model shear-thinning fluid described in Fig. 2. As discussed at the beginning of this section, the ideal operating conditions are in the planar-flow regime, ensuring a fast fill without threatening air entrainment.

In Fig. 13a, we show the critical Reynolds number for the planar-flow and air entrainment transitions as a function of the dimensionless nozzle height, h/D. This parameter has been used in previous studies to understand buckling behaviors [12], as well as air entrainment [20]. While this parameter selection yields a monotonic behavior when the nozzle height h is varied, there is

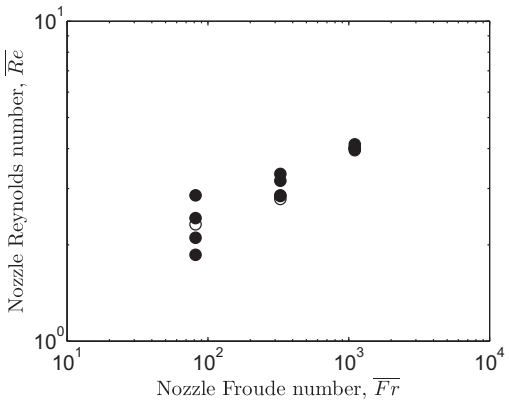

(a) Critical nozzle-based Reynolds number ($\overline{\text{Re}}$) vs. nozzle diameter-based Froude number ($\overline{\text{Fr}}$)

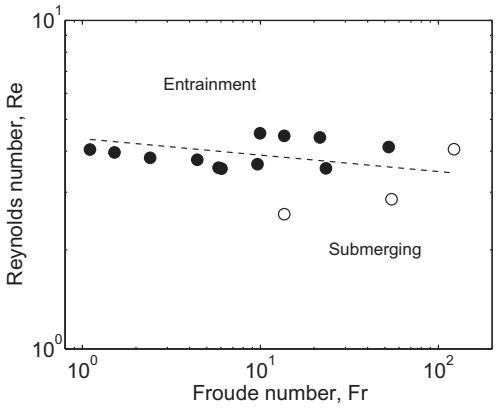

(b) Critical jet-based Reynolds number (Re) vs. jet-based Froude number (Fr)

Fig. 12. Critical entrainment Reynolds number for Newtonian fluids with varied viscosities, nozzle heights, and nozzle diameters. Other geometric parameters as in Table 1. The dashed line is a power-law model, $\text{Re} = 4.36\,\text{Fr}^{-0.05}$. Open symbols represent geometries where $h = 3$ cm.

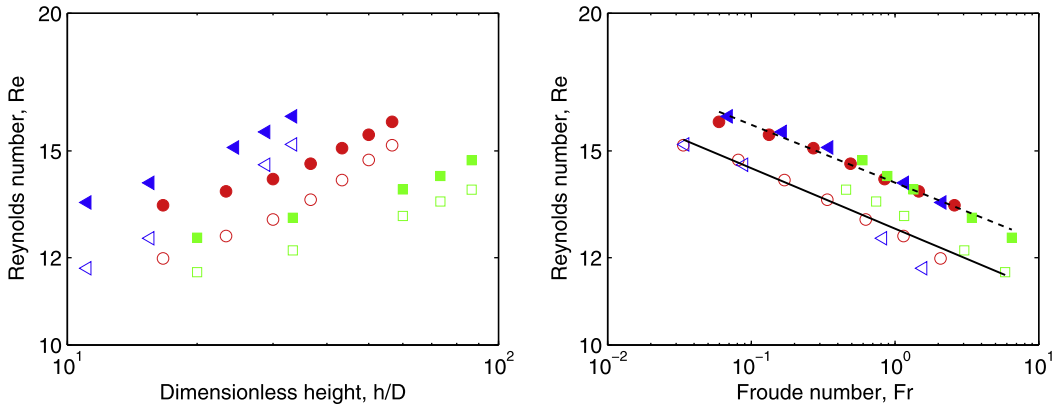

(a) Re vs. Dimensionless height.

(b) Re vs. Fr. Solid line is fit to the planar-flow transition, $\mathrm{Re} = 12.8\mathrm{Fr}^{-0.05}$, and dashed line to the entrainment transition, $\mathrm{Re} = 14.0\mathrm{Fr}^{-0.05}$.

Fig. 13. Critical Reynolds number versus dimensionless numbers for values of h and D. Open symbols represent the planar-flow transition (Fig. 6b) and closed symbols represent the air entrainment transition (Fig. 6d). Nozzle diameters are □ = 0.3 cm, ○ = 0.6 cm, and ◁ = 0.9 cm. Other rheological and geometric parameters are from Table 1.

a systematic deviation when different nozzle diameters D are studied.

A better presentation of these data is by using the Froude number rather than h/D, as shown in Fig. 13b. This parametrization collapses the data, showing that the critical Reynolds number for varied nozzle heights and diameters can be understood through a single scaling. While the pre-factor to the power-law fit to these data varies between the planar-flow and entrainment transitions (as expected), the scaling power is identical ($\mathrm{Re} \sim \mathrm{Fr}^{-0.05}$). This scaling is identical to the Newtonian fluid data shown in Fig. 12. This demonstrates that although the Reynolds numbers are slightly higher for the shear-thinning fluids ($\mathrm{Re} \approx 15$, as compared to $\mathrm{Re} \approx 5$ for Newtonian fluids), the underlying physics behind both systems is similar. Differences in the Reynolds numbers between Newtonian and shear-thinning fluids can be attributed to the major differences in the systems, and the simplifications that are made in characterizing them by a single number. While Newtonian fluids have a constant viscosity throughout the entire flow profile, the viscosity of shear-thinning fluids vary over two orders of magnitude. While we have estimated a characteristic viscosity in Section 3, the actual system is much more complicated.

From a practical standpoint, one interesting observation is that the transition from mounding flow to air entrainment happens very quickly, over a very small range of Reynolds numbers. When these Reynolds numbers are translated back to nozzle velocities, the mean difference between the planar-flow and air entrainment regimes is $\Delta V \approx 10$ cm/s, whereas the actual nozzle velocities can be as high as $V \approx 150$ cm/s, a range of only 10%. This leaves a very small operating window for successful container filling. While the nozzle velocities in systems can range significantly ($50\ \mathrm{cm/s} < V < 150\ \mathrm{cm/s}$), the critical Reynolds number changes very little. This is also of practical importance when designing a container-filling operation, as calculating the Reynolds number will enable a prediction of the ideal operating nozzle velocity for a number of configurations.

With the Reynolds number established as an effective parameter to study both Newtonian and shear-thinning liquids, we can now address the various rheological parameters. The zero-shear viscosity μ_0 is an analog to the Newtonian viscosity discussed in Section 4.1, and can be seen in Fig. 2 at low shear rates. Fig. 14 shows the dependence of the operating window on μ_0. As can be seen from Fig. 14a, increasing μ_0 significantly increases the critical transition velocities. This behavior is consistent with our previous assertion that the critical Reynolds number is approximately constant, as increasing μ_0 increases the characteristic viscosity (12), μ_{jet}. Because of the relatively constant Reynolds numbers shown in Fig. 14b, we expect that inertial forces (i.e. nozzle velocity) must balance viscous forces at the constant Reynolds number, and therefore we expect that the nozzle velocity must rise with increasing μ_0, as is observed. These results further reinforce the choice of the jet-based Reynolds number as the correct parametrization, as it remains relatively constant over a wide range of viscosities and nozzle velocities.

On the other end of the shear-rate spectrum is the infinite-shear viscosity μ_∞, seen at high shear rates in Fig. 2. Because the characteristic shear rates in the vicinity of jet impact, $\dot{\gamma}_{\mathrm{jet}}$, are rarely higher than $10^3\ \mathrm{s}^{-1}$, the local apparent viscosity at impact is typically $\mu_{\mathrm{jet}} \sim O(1\ \mathrm{P})$. Therefore, two regions of behavior are observed when varying μ_∞, shown in Fig. 15. At low shear rates ($\dot{\gamma} < 1\ \mathrm{s}^{-1}$), the characteristic impact viscosity is relatively unaffected by changes to μ_∞, which is reflected by the small changes to the critical nozzle velocities shown in Fig. 15a. However, as μ_∞ increases to near 1 P, the characteristic viscosity begins to increase. This increase in viscosity causes an increase in critical nozzle velocities, as is seen at the higher shear rate in Fig. 15a. In both of these regimes, the Reynolds number remains an effective parameter of the system, as it remains relatively constant.

The shear rate at which the transition from the zero-shear viscosity to the shear-thinning regime begins is determined by λ, and this parameter's effect on the entrainment transitions is shown in Fig. 16. Referring to Fig. 2, as λ increases, the power-law region shifts to lower shear rates. This shift yields a lower characteristic viscosity at the characteristic shear rate (12). In Fig. 16a, a higher value of λ leads to a lower value of the critical velocities, as expected from the lower characteristic viscosities. These deviations can be framed in the context of the Reynolds number and dimensionless characteristic inverse shear rate, shown in Fig. 16b. This figure shows that while the Reynolds number has a slight positive dependence on Wi, the variation is quite small compared to the variation in the nozzle velocity, characterizing the system well.

Similar behavior is seen when examining the effect of the power-law exponent n. As n increases, the slope of the shear-thinning transition (see Fig. 2) increases. This leads to overall higher viscosities for a given shear rate in this thinning region. Fig. 17a exhibits behavior consistent with this analysis as the critical velocities increase with n, while the Reynolds number remains relatively

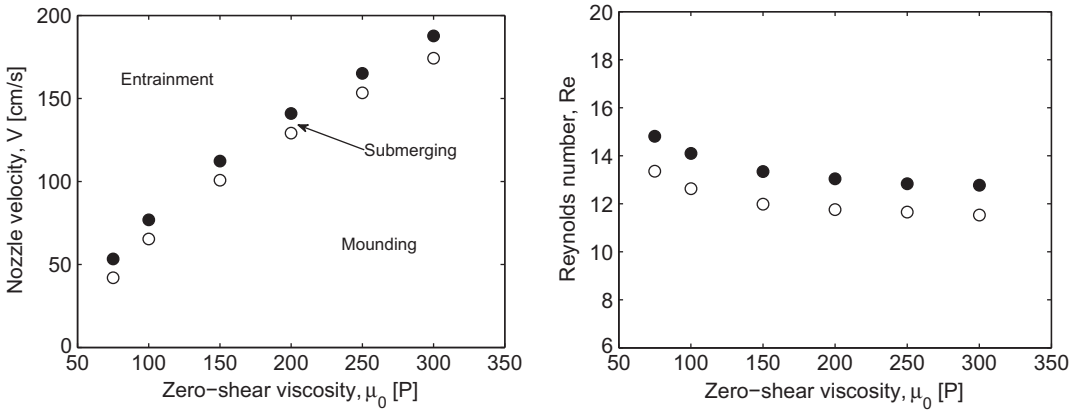

(a) Nozzle velocity vs. μ_0 (b) Reynolds number vs. μ_0

Fig. 14. Transition maps as a function of the zero-shear viscosity, μ_0. Open circles represent the planar-flow transition (Fig. 6b) and closed circles represent the air entrainment transition (Fig. 6d). Base case rheological and geometric parameters are used (Table 1).

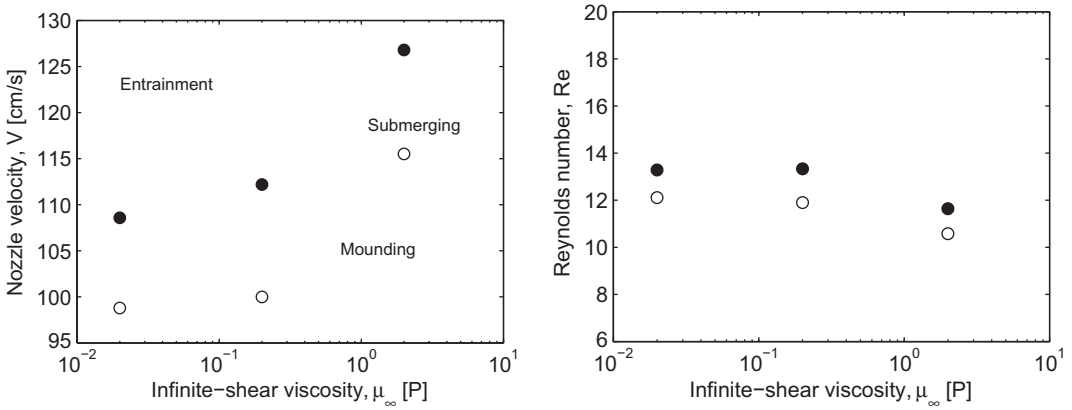

(a) Nozzle velocity vs. μ_∞ (b) Reynolds number vs. μ_∞

Fig. 15. Transition maps as a function of the infinite-shear viscosity, μ_∞. Open circles represent the planar-flow transition (Fig. 6b) and closed circles represent the air entrainment transition (Fig. 6d). Base case rheological and geometric parameters are used (Table 1).

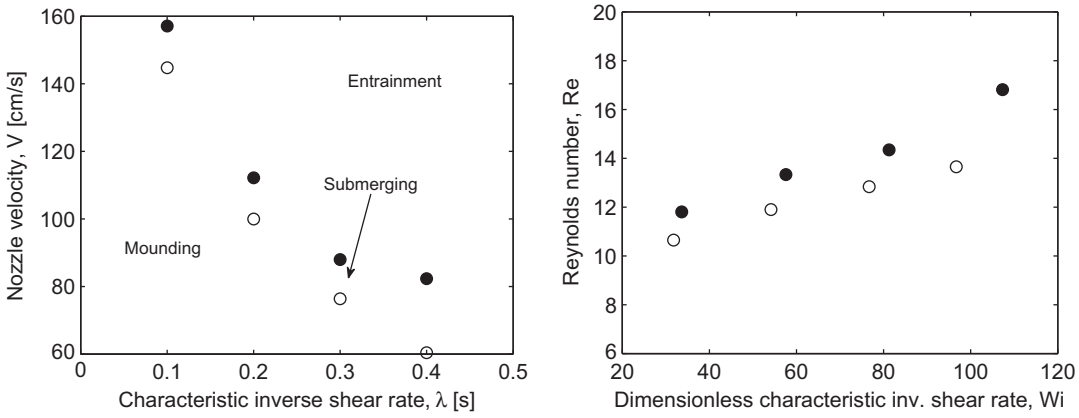

(a) Nozzle velocity vs. λ (b) Reynolds number vs. Wi

Fig. 16. Transition maps as a function of the power-law characteristic inverse shear rate, λ. Fig. 16a represents a comparison using dimensional variables, while 16b uses dimensionless parameters. Open circles represent the planar-flow transition (Fig. 6b) and closed circles represent the air entrainment transition (Fig. 6d). Base case rheological and geometric parameters are used (Table 1).

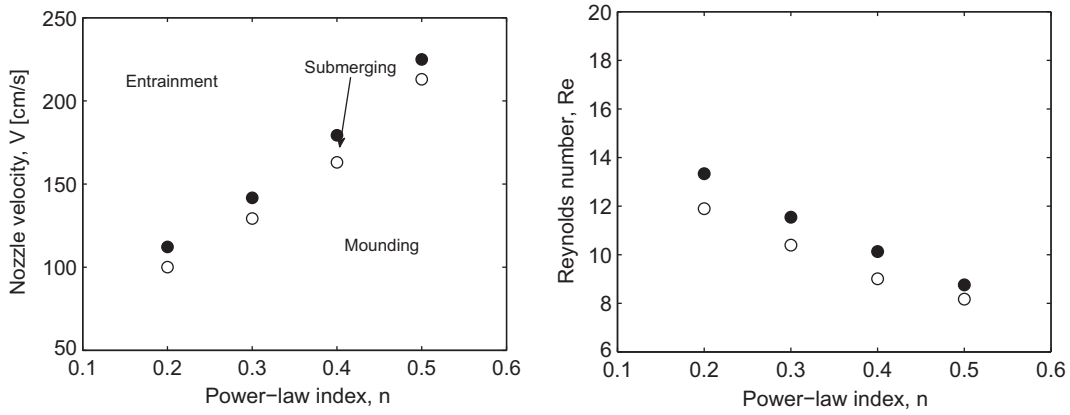

(a) Nozzle velocity vs. n (b) Reynolds number vs. n

Fig. 17. Transitional nozzle velocities as a function of the power-law index, n. Open circles represent the planar-flow transition (Fig. 6b) and closed circles represent the air entrainment transition (Fig. 6d). Base case rheological and geometric parameters are used (Table 1).

constant in Fig. 17b. The slight decrease in the critical Reynolds number with increasing n seen in Fig. 17b is consistent with an asymptotic approach to the Newtonian behavior, which had a critical Reynolds number of $\mathrm{Re} \approx 4$. These results again reinforce our choice of the Reynolds number as an effective parameter for understanding the transitions from mounding to air entrainment.

5. Conclusions

In this paper, we demonstrated that container-filling processes for complex fluid systems can exhibit a wide range of behaviors, and the ideal operating window, in terms of nozzle velocity, can be quite narrow. Experiments and transient 3-D simulations have shown that the interface profiles near the ideal operating conditions are axisymmetric and relatively steady, and so a reduced-order computational model can be useful in determining optimal operating conditions. We proposed a simple steady-state, 2-D axisymmetric FEM model for studying this system. This model was used to determine the ideal filling velocity, deemed the planar flow velocity, and the minimum air entrainment velocity in confined cylindrical geometries.

A suitable scaling of the governing equations suggested a number of dimensionless parameters to use in characterizing these flows. In calculating these dimensionless parameters, choosing the correct scaling parameters can be quite difficult, particularly for shear-thinning fluids, where the viscosity varies over four orders of magnitude. The correct choice of these scalings has a significant effect on the applicability of using these dimensionless numbers to characterize the flow transitions. Our analysis of this system suggests that the key physics occur where the jet impacts the liquid pool, and Bernoulli's equation may be used to estimate the relevant parameters at that location. We showed that the Reynolds and Froude numbers are most useful in characterizing these flows, as they relate the relevant forces: inertial, viscous, and gravitational. Our results also supported the assertion that the key physics occur at the impact region, as our Bernoulli-based scalings led to Reynolds numbers that were relatively constant over a wide range of geometric and rheological parameters.

This model was used to study the transitions from mounding flow to submerging flow to air entrainment for model Newtonian and shear-thinning fluids. We also investigated what effect the container geometry has on the ideal operating conditions. For Newtonian fluids, we found that the presence of a confined container has a significant stabilizing influence over a large unconfined receiving pool. The presence of side walls drastically changes the flow profile, creating "U"-shaped submerged regions with a laminar flow profile in submerging regimes, rather than the thin trumpet shapes with recirculation zones seen previously [18,20,21]. Study of the bath depth shows that when a container is being filled from a nozzle with a constant inlet velocity, air entrainment is more likely to happen late in the filling process, when the bath is deeper, rather than earlier.

For shear-thinning fluids, the critical nozzle velocities were found to be highly dependent on some of the rheological model parameters. While the critical velocities are relatively insensitive to the infinite-shear viscosity, there is a strong trend of higher critical velocities as the zero-shear viscosity increases. The parameters affecting the power-law region of the Carreau model, n and λ, also had a strong influence on the critical velocities. The effect of all of the rheological parameters can be best understood by understanding how they influence the characteristic viscosity at moderate shear rates, $\dot{\gamma} \sim 10^3$. When the characteristic viscosity at the jet impact increases, the inertia necessary to overcome these viscous forces must also increase. The rise in inertia is a result of an increase in the critical nozzle velocities.

When taking all of the data into account, it becomes clear that the relevant physics governing the transition from mounding to submerging flow is a balance between the inertia of the jet and the viscous forces in the receiving pool. While there were slight trends observed in the Reynolds number when certain parameters were varied, overall the Reynolds number remains relatively constant for a wide range of rheological and geometric parameters, identifying it as an important parameter for characterizing these flows.

We have shown that this model should be applicable to many filling operations. However, further experimental validation studies need to be performed to ensure its predictive capability. Also, many industrially relevant fluids exhibit yield-stress or viscoelastic character, and further studies are planned to explore any additional effects these rheological properties may have on container-filling operations.

Acknowledgments

The authors would like to acknowledge The Procter & Gamble Company for support. Thomas Baer was extremely helpful in providing practical suggestions and aided in model preparation. We also appreciate many useful discussions with Dave Dunlop, Anne Grillet, Michael Loewenberg, Gareth McKinley, Lisa Mondy, Christine Roberts, P. Randall Schunk, and Kristianto Tjiptowidjojo.

We also acknowledge Lori Bacca, William Hartt, and Thomas Ober for providing experimental images and Anne Grillet for performing rheological measurements and analysis. The peer reviewers also provided invaluable advice and corrections, and their suggestions much improved this work.

Portions of this work were performed at Sandia National Laboratories. Sandia National Laboratories is a multi program laboratory managed and operated by Sandia Corporation, a wholly owned subsidiary of Lockheed Martin Corporation, for the US Department of Energy's National Nuclear Security Administration under contract DE-AC04-94AL85000.

Appendix A. Details of the numerical method

In this appendix, we detail the numerical algorithm used to arrive at the critical nozzle velocities presented in Section 4. Additionally, we discuss proper selection of the mesh size and the parameter ranges where this model is applicable. Performance of this model is also discussed.

A.1. Mesh sizing and refinement

The computational meshes shown in Fig. 4 are representative of all of the simulations reported in this paper. The nominal size of the element sides at the bottom of container and in the outflow region was $x = 0.15$ cm per side, giving an element area of $x^2 = 0.0225$ cm^2. In the nozzle, jet, and at the free interface near the impact region, however, a more refined mesh is necessary to capture the rapidly changing velocity and viscosity fields, and to accurately capture the shape of the interface. In these areas, the element sides were typically 1/2 to 1/4 of the length, with a length of $x = 0.05$ cm being very typical in the submerging regime shown in Fig. 4b.

To confirm the validity of the interface shapes for the typical mesh, a mesh refinement study was conducted on two meshes with constant nominal element size, with results shown in Figs. 18, 19. Two measures are key for the accurate modeling of this problem. First, as there are regions within the system that have highly varying apparent viscosities, accurate spatial resolution of these viscosities must be captured. Fig. 18 shows the L_2 norm of the viscosity, which gives an overall measure of the accurate spatial resolution of the viscosity changes, with increasing mesh resolution. As the mesh size decreases, the resolution increases and the L_2 norm appears to converge to the "correct" value, determined by the most highly-refined mesh (side length of $x = 0.025$ cm). It is important to note, however, that most of the cases shown in Fig. 18 are within 1% of the "correct" value, so there is high confidence in the spatial resolution for the mesh sizes used in this work.

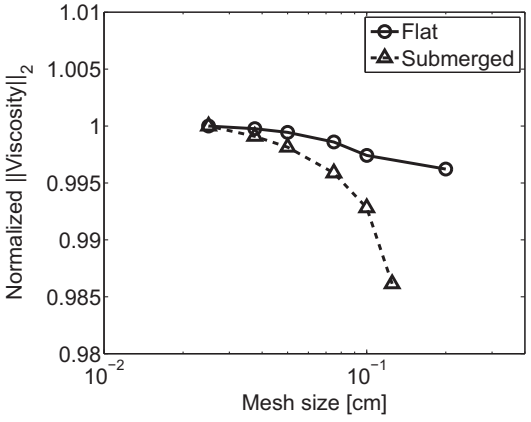

Fig. 18. L_2 norm of the viscosity for various levels of mesh refinement, normalized by the L_2 norm for the most refined mesh of side length $x = 0.025$ cm. Results for two profiles are presented, one for a flat interface, shown in Fig. 19a, and the other for a submerged interface, shown in Fig. 19b.

The other key measure is the accuracy in which the mesh can capture the true shape of the free interface, particularly near the jet impact. This measure is important, as it is used to determine the transition velocities presented in this paper. Fig. 19 compares the interface shape for two levels of mesh refinement in two different flow regimes, with Fig. 19a showing a flat interface and Fig. 19b showing a submerged interface. In these illustrations, the 2-D mesh has a nominal element side length $x = 0.1$ cm, while the interface shape for a more highly refined mesh, with nominal element side length $x = 0.025$ cm, is shown as the darker line. As shown in Fig. 19a, the less refined mesh nearly perfectly captures the true interface shape for the flat interface. For the submerged case in 19b, the interface is mostly captured by the coarse mesh, with the exception of slight deviations at the bottom of the dip. Refining the mesh to $x = 0.5$ cm, however, allows for a smooth representation of the interface.

A.2. Continuation and convergence algorithm

Obtaining the initial converged solution for a given geometry and rheology is a multi-step process, which we describe in detail here.

1. Prepare the initial mesh, similar to Fig. 4a, with the desired geometry, including nozzle radius r, nozzle height h, container radius W, and container height L.
2. Holding the mesh fixed, converge a simulation for a Newtonian fluid at a low nozzle velocity. If a simulation of a Carreau fluid is the final goal, use the zero-shear viscosity μ_0 as the Newtonian viscosity. In this context, a "low" nozzle velocity is a velocity that is expected to be well within the mounding regime for the final simulation, and must be selected with some prior intuition as to what it should be, or by trial and error.
3. Using the solution from step 2 as the initial guess, reinstate the kinematic boundary condition, allowing the mesh to deform, and converge a Newtonian free-interface solution.
4. Remesh the converged solution from step 3 using the remeshing procedure described in A.2.1.
5. For simulations of Carreau fluids, use the first-order continuation algorithm described in Section 2.4 to decrease the shear-thinning parameter n until the desired rheological parameters are converged. This process may take anywhere from 5 to 30 steps, depending on the difficulty of the simulation, and the continuation step size is dynamically adjusted to maximize step size while ensuring convergence of each steady-state solution. Occasionally throughout this continuation process, the interface shape will deform significantly enough to warrant interim remeshing (see A.2.1). The final converged solution is also remeshed and should be in the "mounding" regime.
   Using this method, we are regularly able to converge simulations with n as low as 0.2. While it may be possible to converge for even lower values, the problem becomes much more computationally challenging, requiring much smaller continuation steps and more "tricks" to converge the Newton iterations. However, for the fluids of interest in this study, $n = 0.2$ fits the available rheological data well, and continuation lower than $n = 0.2$ is unnecessary.
6. In order to determine the critical nozzle velocities described in Section 4, the first-order continuation algorithm is used to increase the nozzle velocity V in small steps, observing the progression of the interface shape. The converged and remeshed solution from step 5 is used as the initial guess for this process.

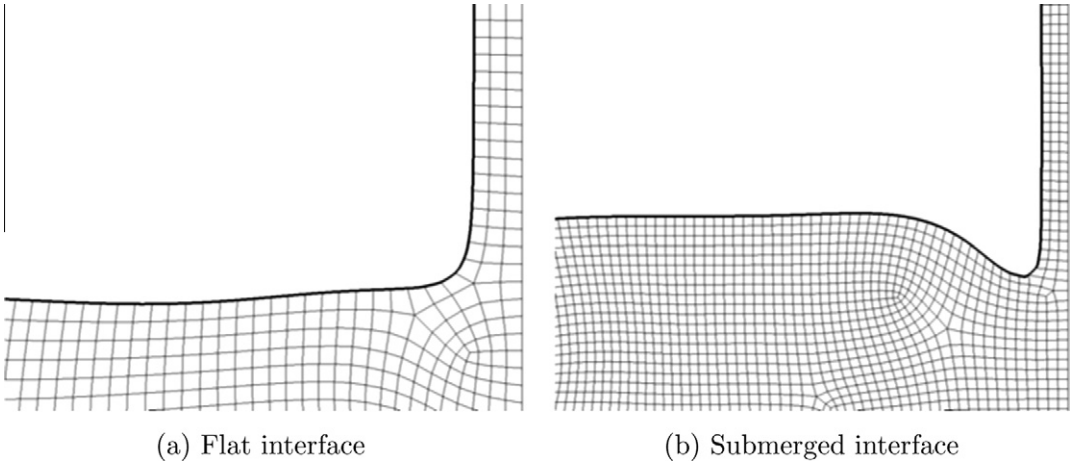

Fig. 19. Interface profiles shown for two levels of mesh refinement. The entire mesh is shown for mesh size x = 0.1 cm, while a thick line at the interface is shown for the most refined mesh, x = 0.025 cm.

Multiple interim remeshing steps (see A.2.1) are performed throughout the continuation as the mesh deforms significantly. The "flat" (Fig. 6b) and "entrainment" (Fig. 6d) flow profiles are identified visually and the velocity at which these profiles occur are recorded for analysis.

7. In addition to continuing in nozzle velocity, simulations for different geometric and rheological parameters can be obtained without repeating all steps 1–5, but instead taking a converged solution from step 5 and using the continuation algorithm to slowly vary the desired parameter. This method was used to obtain the majority of results in Section 4 and is much more efficient than repeating the entire procedure for each set of parameters.

A.2.1. Remeshing schemes

Occasionally during this continuation process (steps 4–7), geometry evolution leads to excessive mesh distortion, where the nodes of individual mesh elements cross mesh lines or become co-linear. Too much distortion undermines the numerical accuracy and convergence of the method. To prevent this, the mesh is monitored throughout the continuation process, and when poorly shaped elements are observed, the simulation is paused. The deformed geometry is then re-meshed in Cubit [42] using the same criteria used to generate the initial mesh. The solution from the deformed solution is then mapped onto the newly meshed geometry, and the continuation process is resumed. If the mesh deforms too much during this continuation process, it may be difficult, or even impossible, to obtain a valid solution upon restart. Therefore, care must be taken to monitor the mesh deformation and pause at any sign of overly-deformed elements.

A.2.2. Relaxed Newton iterations

Oftentimes, the equations are sufficiently nonlinear or the initial guess is sufficiently far away from the true solution that simulations will not converge under full-Newton iterations. To address this issue, Goma has implemented a dynamically adaptive, relaxed Newton iteration scheme that can greatly increase the range of convergence of this algorithm. In this method, the Newton iteration formula is

$$\mathbf{x}_{i+1} = \mathbf{x}_i - r\frac{\mathbf{R}_i}{\partial \mathbf{R}_i/\partial \mathbf{x}_i}, \tag{15}$$

where $\boldsymbol{x}$ is the solution vector, $\boldsymbol{R}$ is the residual vector, i is the iteration counter, and r is the relaxation parameter, with r<1 relaxing the iteration and r=1 representing a full-Newton iteration. The value of r is dynamically chosen depending on the L_2 norm of the residual vector, which represents how close the iterations are to convergence. The relaxation parameter r can start off low ($r \sim 0.1$) and increase as the iterations near convergence. However, a typical set of parameters for this scheme is r=0.6 for the L_2 norm $> 10^{-3}$, r=0.8 for the L_2 norm $> 10^{-4}$, and r=1.0 for the L_2 norm $< 10^{-4}$.

A.3. Performance

A key advantage to the use of this reduced-order model is the reduction in time necessary to perform the analysis for a wide range of geometric and rheological parameters. Simulation times can vary widely, depending on the difficulty of the problem and complexity of interface shape. However, an average steady-state simulation takes approximately 1–3 minutes to converge, with the longest times being required when strong relaxation of the Newton iterations (A.2.2) is necessary. While there are many steps to the entire presented in A.2, this entire process (steps 1–6) is contained in a script and is mostly automated. Typical run times for this algorithm are 2–3 h. However, through the use of step 7, converged solution can be used to significantly reduce this time to approximately 1 hour in some instances. This total simulation time is significantly shorter than the times required to run the 3-D transient validation simulations shown in Fig. 8, which often require 24–48 h on an eight-core machine.

References

[1] P. Doshi, R. Suryo, O.E. Yildirim, G.H. McKinley, O.A. Basaran, Scaling in pinch-off of generalized newtonian fluids, J. Non-Newtonian Fluid Mech. 113 (2003) 1–27.
[2] P. Doshi, O.A. Basaran, Self-similar pinch-off of power law fluids, Phys. Fluids 16 (2004) 585–593.
[3] R. Suryo, O.A. Basaran, Local dynamics during pinch-off of liquid threads of power law fluids: scaling analysis and self-similarity, J. Non-Newtonian Fluid Mech. 138 (2006) 134–160.
[4] O.E. Yildirim, O.A. Basaran, Dynamics of formation and dripping of drops of deformation-rate-thinning and -thickening liquids from capillary tubes, J. Non-Newtonian Fluid Mech. 136 (2006) 17–37.
[5] J.W.M. Bush, J.M. Aristoff, The influence of surface tension on the circular hydraulic jump, J. Fluid Mech. 489 (2003) 229–238.
[6] T.T. Hsu, T.W. Walker, C.W. Frank, G.G. Fuller, Role of fluid elasticity on the dynamics of rinsing flow by an impinging jet, Phys. Fluids 23 (2011) 033101.
[7] J.O. Cruickshank, B.R. Munson, Viscous fluid buckling of plane and axisymmetric jets, J. Fluid Mech. 113 (1981) 221–239.
[8] J.O. Cruickshank, B.R. Munson, A theoretical prediction of the fluid buckling frequency, Phys. Fluids 26 (1983) 928–930.
[9] B. Tchavdarov, A.L. Yarin, S. Radev, Buckling of thin liquid jets, J. Fluid Mech. 253 (1993) 593–615.

[10] M. Tomé, A. Filho, J. Cuminato, N. Mangiavacchi, S. McKee, GENSMAC3D: a numerical method for solving unsteady three-dimensional free surface flows, Int. J. Numer. Methods Fluids 37 (2001) 747–796.
[11] M.F. Tomé, N. Mangiavacchi, J.A. Cuminato, A. Castelo, S. McKee, A finite difference technique for simulating unsteady viscoelastic free surface flows, J. Non-Newtonian Fluid Mech. 106 (2002) 61–106.
[12] N.M. Ribe, A general theory for the dynamics of thin viscous sheets, J. Fluid Mech. 457 (2002) 255–283.
[13] N.M. Ribe, Coiling of viscous jets, Proc. R. Soc. Lond. A 460 (2004) 3223–3239.
[14] N.M. Ribe, M. Habibi, D. Bonn, Stability of liquid rope coiling, Phys. Fluids 18 (2006) 084102.
[15] C.M. Oishi, M.F. Tomé, J.A. Cuminato, S. McKee, An implicit technique for solving 3D low Reynolds number moving free surface flows, J. Comput. Phys. 227 (2008) 7446–7468.
[16] M. Habibi, Y. Rahmani, D. Bonn, N.M. Ribe, Buckling of liquid columns, Phys. Rev. Lett. 104 (2010) 074301.
[17] T.J. Lin, Gas Bubble Entrainment by Plunging Laminar Liquid Jets, Ph.D. thesis, Wayne State University, 1963.
[18] T.J. Lin, H.G. Donnelly, Gas bubble entrainment by plunging laminar liquid jets, AIChE J. 12 (1966) 563–571.
[19] A. Bin, Minimum air entrainment velocity of vertical plunging liquid jets, Chem. Eng. Sci. 43 (1988) 379–389.
[20] A.K. Bin, Gas entrainment by plunging liquid jets, Chem. Eng. Sci. 48 (1993) 3585–3630.
[21] E. Lorenceau, D. Quéré, J. Eggers, Air entrainment by a viscous jet plunging into a bath, Phys. Rev. Lett. 93 (2004) 254501.
[22] D.H. Johnson (Ed.), Hair and Hair Care, CRC Press, p. 345.
[23] L. Bacca, W. Hartt, T. Ober, Experimental images for mounding and submerging flows, Private communication (2010).
[24] G.I. Taylor, Instability of jets threads and sheets of viscous fluid, Proc. Int. Congr. Appl. Mech. (1969) 382.
[25] M.F. Tomé, A. Castelo, J. Murakami, J.A. Cuminato, R. Minghim, M.C.F. Oliveira, N. Mangiavacchi, S. McKee, Numerical simulation of axisymmetric free surface flows, J. Comput. Phys. 157 (2000) 441–472.
[26] Y. Zhu, H.N. Oğuz, A. Prosperetti, On the mechanism of air entrainment by liquid jets at a free surface, J. Fluid Mech. 404 (2000) 151–177.
[27] H. Chanson, T. Brattberg, Air entrainment by two-dimensional plunging jets: the impingement region and the very-near flow field, in: ASME Fluids Engineering Division Summer Meeting.
[28] M. El Hammoumi, J.L. Achard, L. Davoust, Measurements of air entrainment by vertical plunging liquid jets, Exp. Fluids 32 (2002) 624–638.
[29] M.F. Tomé, S. McKee, Numerical simulation of viscous flow: buckling of planar jets, Int. J. Numer. Methods Fluids 29 (1999) 705–718.
[30] M. Tomé, S. McKee, L. Barratt, D. Jarvis, A. Patrick, An experimental and numerical investigation of container filling with viscous liquids, Int. J. Numer. Methods Fluids 31 (1999) 1333–1353.
[31] A.N. Alexandrou, E. Duc, V. Entov, Inertial, viscous and yield stress effects in bingham fluid filling of a 2-D cavity, J. Non-Newtonian Fluid Mech. 96 (2001) 383–403.
[32] A.N. Alexandrou, P.L. Menn, G. Georgiou, V. Entov, Flow instabilities of Herschel–Bulkley fluids, J. Non-Newtonian Fluid Mech. 116 (2003) 19–32.
[33] R.B. Bird, O. Hassager, Dynamics of Polymeric Liquids, second ed., Volume 1: Fluid Mechanics, Wiley-Insterscience, 1987.
[34] D. Silagy, Y. Demay, J.F. Agassant, Stationary and stability analysis of the film casting process, J. Non-Newtonian Fluid Mech. 79 (1998) 563–583.
[35] F. Rousset, S. Millet, V. Botton, H.B. Hadid, Temporal stability of Carreau fluid flow down an incline, J. Fluids Eng. 129 (2007) 913–920.
[36] R. Valette, P. Laure, Y. Demay, J.-F. Agassant, Convective linear stability analysis of two-layer coextrusion flow for molten polymers, J. Non-Newtonian Fluid Mech. 121 (2004) 41–53.
[37] S.A. Roberts, S. Kumar, Stability of creeping couette flow of a power-law fluid past a deformable solid, J. Non-Newtonian Fluid Mech. 139 (2006) 93–102.
[38] D.J. Coyle, C.W. Macosko, L.E. Scriven, Film-splitting flows of shear-thinning liquids in forward roll coating, AIChE J. 33 (1987) 741–746.
[39] C. Lawrence, W. Zhou, Spin coating of non-Newtonian fluids, J. Non-Newtonian Fluid Mech. 39 (1991) 137–187.
[40] K.-T. Kim, R.E. Khayat, Transient coating flow of a thin non-Newtonian fluid film, Phys. Fluids 14 (2002) 2202–2215.
[41] J. Eggers, Universal pinching of 3D axisymmetric free-surface flow, Phys. Rev. Lett. 71 (1993) 3458–3460.
[42] T. Blacker, W. Bohnhoff, T. Edwards, CUBIT Mesh Generation Environment, vol. 1: Users manual, Technical Report SAND–94-1100, Sandia National Laboratories, 1994. <http://cubit.sandia.gov>.
[43] P.A. Sackinger, P.R. Schunk, R.R. Rao, A Newton–Raphson pseudo-solid domain mapping technique for free and moving boundary problems: a finite element implementation, J. Comput. Phys. 125 (1996) 83–103.
[44] R.A. Cairncross, P.R. Schunk, T.A. Baer, R.R. Rao, P.A. Sackinger, A finite element method for free surface flows of incompressible fluids in three dimensions. Part I. Boundary fitted mesh motion, Int. J. Numer. Methods Fluids 33 (2000) 375–403.
[45] H. Saito, L.E. Scriven, Study of coating flow by the finite element method, J. Comput. Phys. 42 (1981) 53–76.
[46] S.F. Kistler, L.E. Scriven, Coating flows, in: J.R.A. Pearson, S.M. Richardson (Eds.), Applied Science Publishers, London, 1983, pp. 243–299.
[47] K.N. Christodoulou, L.E. Scriven, Discretization of free surface flows and other moving boundary problems, J. Comput. Phys. 99 (1992) 39–55.
[48] T. Patzek, R. Benner Jr, O. Basaran, L. Scriven, Nonlinear oscillations of inviscid free drops, J. Comput. Phys. 97 (1991) 489–515.
[49] O.A. Basaran, Nonlinear oscillations of viscous liquid drops, J. Fluid Mech. 241 (1992) 169–198.
[50] O.A. Basaran, D.W. DePaoli, Nonlinear oscillations of pendant drops, Phys. Fluids 6 (1994) 2923–2943.
[51] E.D. Wilkes, S.D. Phillips, O.A. Basaran, Computational and experimental analysis of dynamics of drop formation, Phys. Fluids 11 (1999) 3577–3598.
[52] T.-Y. Chen, J. Tsamopoulos, Nonlinear dynamics of capillary bridges: theory, J. Fluid Mech. 255 (1993) 373–409.
[53] S. Dodds, M.S. Carvalho, S. Kumar, Stretching and slipping of liquid bridges near plates and cavities, Phys. Fluids 21 (2009) 092103.
[54] P.R. Schunk, P.A. Sackinger, R.R. Rao, K.S. Chen, T. Baer, D.A. Labreche, A.C. Sun, M.M. Hopkins, S.R. Subia, H.K. Moffat, R.B. Secor, R.A. Roach, E.D. Wilkes, D.R. Noble, P.L. Hopkins, P.K. Notz, GOMA 5.0 – A Full-Newton Finite Element Program for Free and Moving Boundary Problems with Coupled Fluid/Solid Momentum, Energy, Mass, and Chemical Species Transport: User's Guide, Technical Report SAND2006-5375, Sandia National Laboratories, 2006.
[55] H.D. Rowland, A.C. Sun, P.R. Schunk, W.P. King, Impact of polymer film thickness and cavity size on polymer flow during embossing: toward process design rules for nanoimprint lithography, J. Micromech. Microeng. 15 (2005) 2414.
[56] H.D. Rowland, W.P. King, A.C. Sun, P.R. Schunk, G.L.W. Cross, Predicting polymer flow during high-temperature atomic force microscope nanoindentation, Macromolecules 40 (2007) 8096–8103.
[57] M. Heroux, R. Bartlett, V.H.R. Hoekstra, J. Hu, T. Kolda, R. Lehoucq, K. Long, R. Pawlowski, E. Phipps, A. Salinger, H. Thornquist, R. Tuminaro, J. Willenbring, A. Williams, An Overview of Trilinos, Technical Report SAND2003-2927, Sandia National Laboratories, 2003. <http://trilinos.sandia.gov/>.
[58] X.S. Li, J.W. Demmel, SuperLU_DIST: a scalable distributed-memory sparse direct solver for unsymmetric linear systems, ACM Trans. Math. Softw. 29 (2003) 110–140.
[59] E. Allgower, K. Georg, Introduction to numerical continuation methods, Soc. Ind. Math. (2003).
[60] R.L. Panton, Incompressible Flow, third ed., Wiley, 2005.
[61] Flow Science Inc., Santa Fe, NM, FLOW-3D, 2010. <http://www.flow3d.com>.
[62] OpenCFD Ltd., OpenFOAM, Online, 2010. <http://www.openfoam.com>.